NeuroImage 185 (2019) 119–128

Contents lists available at ScienceDirect

NeuroImage

journal homepage: www.elsevier.com/locate/neuroimage

Axons morphometry in the human spinal cord

Tanguy Duval [a], Ariane Saliani [a], Harris Nami [a], Antonio Nanci [b], Nikola Stikov [a,c], Hugues Leblond [d], Julien Cohen-Adad [a,e,*]

[a] NeuroPoly Lab, Institute of Biomedical Engineering, Polytechnique Montreal, Montreal, QC, Canada
[b] Laboratory for the Study of Calcified Tissues and Biomaterials, Faculty of Dental Medicine, University of Montreal, Montreal, QC, Canada
[c] Montreal Heart Institute, Montreal, QC, Canada
[d] Anatomy department, Université du Québec à Trois-Rivières, Trois-Rivières, QC, Canada
[e] Functional Neuroimaging Unit, CRIUGM, Université de Montréal, Montréal, QC, Canada

A B S T R A C T

Due to the technical challenges of large-scale microscopy and analysis, to date only limited knowledge has been made available about axon morphometry (diameter, shape, myelin thickness, volume fraction), thereby limiting our understanding of neuronal microstructure and slowing down research on neurodegenerative pathologies. This study addresses this knowledge gap by establishing a state-of-the-art acquisition and analysis framework for mapping axon morphometry, and providing the first comprehensive mapping of axon morphometry in the human spinal cord.

We dissected, fixed and stained a human spinal cord with osmium tetroxide, and used a scanning electron microscope to image the entirety of 23 axial slices, covering C1 to L5 spinal levels. An automatic method based on deep learning was then used to segment each axon and myelin sheath to produce maps of axon morphometry. These maps were then registered to a standard spinal cord magnetic resonance imaging (MRI) template.

Between 500,000 (lumbar) and 1 million (cervical) myelinated axons were segmented at each level of this human spinal cord. Morphometric features show a large disparity between tracts, but high right-left symmetry. Our results suggest a modality-based organization of the dorsal column in the human, as it has been observed in the rat. The generated axon morphometry template is publicly available at https://osf.io/8k7jr/ and could be used as a reference for quantitative MRI studies. The proposed framework for axon morphometry mapping could be extended to other parts of the central or peripheral nervous system that exhibit coherently-oriented axons.

1. Introduction

The so-called “white matter” in the central nervous system is composed of long projections of the nerve cells, the axons, that transmit neural impulses. Surrounded by a myelin sheath that enables faster conduction at higher firing rates, these fibers (axon plus the surrounding myelin sheath) are grouped into bundles that interconnect different regions of the central and peripheral nervous system. Myelinated and unmyelinated fibers together occupy about 60% of the white matter volume (Mottershead et al., 2003; Perge et al., 2009), and the rest is occupied mostly by glial cells and blood vessels. The morphometry of white matter axons is remarkably heterogeneous: reported sizes range between 0.1 and 10 μm (Perge et al., 2012). It also appears that different white matter pathways have different microstructural characteristics (Nieuwenhuys et al., 2007), but to date this observation has mostly been qualitative, and there are limited data that clearly describe and quantify these differences, and how much these fibers vary across human populations in the brain (Walhovd et al., 2014) and spinal cord (Saliani et al., 2017; Watson et al., 2009).

Traumatic injuries or neurodegenerative diseases such as multiple sclerosis can damage the axons, potentially leading to chronic pain and functional deficits such as paraplegia. The limited knowledge that we have about white matter microstructure is problematic for understanding what happens at the micro- and macroscopic levels under pathological conditions such as multiple sclerosis. In particular, quantitative information on the axonal microstructure is needed in order to validate the accuracy of non-invasive microstructure imaging methods used for the diagnosis and prognosis of these pathologies (Cohen-Adad and Wheeler-Kingshott, 2014; Dula et al., 2010; Duval et al., 2017).

If we look specifically at the spinal cord, recent anatomy books (Gray et al., 2005; Nieuwenhuys et al., 2007; Watson et al., 2009) suggest that knowledge about fiber organisation in the white matter is an accumulation of decades of research by neuroanatomists and it is not uncommon to use as a references studies that are over fifty years old (Demyer, 1959; Gray, 1867; Lassek, 1945; Verhaart, 1962). Indeed, mapping and classifying the connection and the morphometry of millions of fibers requires

* Corresponding author. NeuroPoly Lab, Institute of Biomedical Engineering, Polytechnique Montreal, Montreal, QC, Canada.
E-mail address: jcohen@polymtl.ca (J. Cohen-Adad).

https://doi.org/10.1016/j.neuroimage.2018.10.033
Received 20 March 2018; Received in revised form 5 October 2018; Accepted 10 October 2018
Available online 13 October 2018

particularly painstaking studies that cannot easily be reproduced. While the entire spinal cord cytoarchitecture has been described qualitatively (Nieuwenhuys et al., 2007), fiber volume fraction and size have been measured quantitatively only in specific tracts. Furthermore, because each tract is generally studied by different authors who employ different methodologies (tissue preparation, imaging system), a quantitative inter-tract comparison is difficult. Another major issue is that the methodology of these pioneer studies is questionable: for instance, staining based on silver impregnation prevents researchers from differentiating axon and glial processes (Wada et al., 2001), leading to an overestimation of the axonal density (axons per mm^2) by a factor 10 to 20 (Wada et al., 2001). An extensive review of axon morphometry in the spinal cord can be found in Saliani et al., (2017).

Recent improvements in microscopy hardware and storage capacity have resulted in the emergence of large field of view imaging (e.g. full mouse brain) at a single-axon resolution (Hua et al., 2015; Mikula et al., 2012; Mikula and Denk, 2015), along with the development of automatic software to segment these datasets (Bégin et al., 2014; Sommer et al., 2011; Zaimi et al., 2018, 2016).

In this work, we establish an acquisition and analysis framework for mapping axons in the central nervous system and demonstrate its application in an ex vivo human spinal cord. Following post mortem extraction of the cord, 23 axial planes were imaged using a scanning electron microscope (SEM) at a resolution of 130–260 nm/px, resulting in images comprised of approximately 10 gigapixels, covering the cervical to lumbar spinal levels. Axons and their myelin sheaths were automatically segmented using deep learning (Zaimi et al., 2018) in order to derive quantitative measures of axonal diameter, axonal volume fraction and myelin volume fraction. Finally, global statistics evaluated the differences between levels, left *versus* right tracts and ascending *versus* descending (sensory/motor) tracts. Maps of axon morphometry were combined and registered to a spinal cord template to create the first microstructure atlas of the human spinal cord white matter.

2. Methods

2.1. Tissue preparation

Cadaver. The spinal cord was extracted from the fresh cadaver of a 71 year-old female (1.60 m tall, weight 55 Kg, right-handed), donated to the anatomy laboratory at the University du Québec at Trois-Rivières by informed consent. The donor died of pneumonia and was diagnosed with disseminated lupus erythematosus, a myocarditis, diabetes mellitus and cold agglutinin. No macroscopic anomaly of the vertebral column or spinal cord (e.g. spondylosis) was found at dissection. All procedures were approved by the local Ethics Committee (SCELERA-15-03-pr01).

Dissection. Two hours after death, the spinal cord was dissected and cut into 5–10 mm thick transverse sections (see Fig. 1). The rostro-caudal position was estimated by counting the nerve roots (8 cervical, 12 thoracic and 5 lumbar). The right side of the spine was marked using strings attached to the nerve roots. 30 samples were extracted, but 6 samples were rendered unusable due to staining and cutting issues, and one sample due to acquisition issues (bad focus).

Fixation. Just after dissection, samples were immersed in separate 50 mL vials containing a solution of 4% paraformaldehyde and 0–2% glutaraldehyde (see Table 1), and stored at 4 °C. The buffer was a PBS 1x solution, adjusted for a pH of 7.4 with HCl. Different glutaraldehyde concentrations were used in order to assess the bias to tissue shrinkage (see discussion). After a week, samples were transferred to PBS 1x to prevent over-fixation. Table 1 lists the extracted spinal cord sections, their spinal level, and the exact glutaraldehyde concentrations.

Preparation for microscopy. Samples were stained with osmium tetroxide 2% over 10 h in 10 mL vials. A bidirectional rotator was used to prevent deposition of the osmium at the bottom of the vial. Samples were then washed in distilled water, and dehydrated in 10, 25, 50, 75 and 100% acetone baths for 30 min each. Acetone was then progressively replaced with 50 and 100% Epon 812 (Mecalab, Canada) for 12 h each. Final embedding was done at 60 °C for 24 h. During the final embedding, each axial slice was carefully positioned at the bottom of the mold, and maintained using a plastic grid, in order to have the surface as flat as possible. Once the embedding procedure was finished, a microtome (Reichert-Jung) was used to remove the first layers of resin (15 µm thickness) in order to expose the entire slice of spinal cord (see Fig. 2). The large tungsten-carbide blade of the microtome could cut the entire block by layers of 15 µm. When the cord surface was found to bulge slightly, which is bound to happen with such large ($1 \times 1x0.2\ cm^3$) samples, we performed the cutting at various angles. During the procedure, the spots of the tissue already exposed were carefully avoided by changing the cutting angle. This procedure was necessary to prevent from cutting deeper than 200 µm at these specific spots, which corresponds to the penetration depth of osmium (Hua et al., 2015). About 50–100 µm of tissue was uniformly removed before obtaining fully exposed slices of spinal cord. Exposed slices of spinal cord were then polished using a

Fig. 1. Spinal cord dissection. The spinal cord was first entirely exposed (Left) and 30 half-to 1-cm thick slices of spinal cord were extracted and post-fixed in separate large (50 mL) flasks (right). Note that only 23 samples were finally used for the present study.

Table 1
List of samples. C: cervical level, T: thoracic level and L: lumbar level. When multiple slices were extracted at the same level, letters A, B and C were used with A being the most rostral slice.

spinal level	Glutaraldehyde	SEM resolution (nm)
C1A	0%	260
C1B	0%	260
C2A	2%	130
C2B	0%	260
C2C	0.5%	130
C3A	2%	130
C3B	0.5%	130
C3C	0%	260
C4A	2%	130
C5A	0.5%	130
C5B	2%	130
C6A	0.5%	130
C6B	2%	130
C7B	0.5%	130
T6	2%	130
T9	0.5%	130
T12	0%	260
L1	0.5%	130
L2A	2%	130
L2B	0%	260
L3A	0.5%	130
L4A	0%	260
L5	0%	260

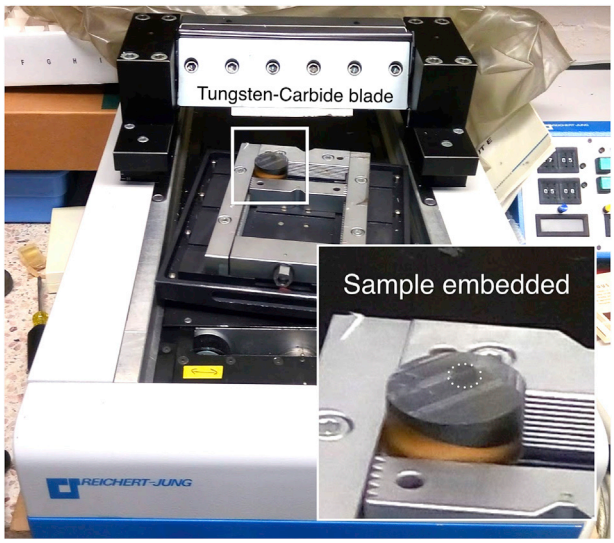

Fig. 2. Microtomy. A Tungsten-Carbide blade was used to expose the surface of the spinal cord. The support angle was varied in order to prevent from cutting deeper than 100 µm.

0.05 µm aluminum polishing suspension, and electrical conduction was ensured using vapor deposition of gold (layer of 600 Å).

2.2. Microscopy

Images were obtained using an SEM system (JEOL JSM7600F) controlled with AZtec 3.2 software (Oxford Instruments, UK). Each sample was carefully positioned on the specimen holder to ensure a parallel surface and good conduction with the specimen holder using carbon tape. The large area mapping solution of AZtec was used to acquire a mosaic of 150–300 sub-images (depending on the spinal level) of $1060 \times 729\ \mu m^2$ each, at a resolution of 130 nm/px (8192 × 5632 pixels/sub-image) or 260 nm/px (4096 × 2816) (see Table 1). The following parameters were used for the scanning: low magnification mode, low-angle backscattered electron detector (LABE), aperture of 110 µm, acceleration voltage of 15 kV, probe current 10 nA, 110× magnification, 15 mm distance, 2 µs dwell time. Low magnification mode was selected to increase the field of view and the depth of field. Focus was set in the peripheral nerves to prevent surface degradation, and the contrast/brightness was manually adjusted. If the signal-to-noise ratio was not satisfactory, the scanning distance was reduced to 10 mm and the probe current increased to 11 nA.

2.3. Image processing

Stitching. Mosaics were formed automatically by stitching the sub-images together using the *Grid/Collection Stitching Plugin* (Preibisch et al., 2009) of the image processing program Fiji (Schindelin et al., 2012). Because the stitching was failing in some regions (usually at the periphery of the spinal cord where the background is present), an outlier detection was implemented assuming a constant shift of the stage (see supplementary material 7.1).

Segmentation. Axons and myelin of each sub-image of the mosaic were automatically segmented using AxonDeepSeg (v0.2) (Zaimi et al., 2018) on a computer equipped with a 12-core Xeon Phi processor. The segmentation of a full slice of spinal cord was obtained in about 2 h using the SEM model that is included in the software. For each axon, the following properties were measured:

- Axon diameter: $d = 2\sqrt{A_{axon}/\pi}$ (A_{axon} is the area of the segmented axon)
- Fiber diameter: $D = 2\sqrt{A_{fiber}/\pi}$ ($A_{fiber} = A_{myelin} + A_{axon}$)
- g-Ratio: $g = \frac{d}{D}$
- eccentricity: $e = \frac{\sqrt{a^2-b^2}}{a}$ (with a the length of the major axis and b the length of the minor axis of the ellipse that has the same normalized second central moments as the segmented axon (Haralick and Shapiro, 1992, Appendix A))

In order to prevent over- or under-segmentation, segmentation biases were compensated by comparing manual segmentations (ground truth) and automatic segmentations on a region of $1 \times 0.5\ mm^2$. See supplementary material 7.2 for more details. Note that axons smaller than 1 µm were mostly false positives (see discussion about "resolution limit"), and were removed from the reported average metrics.

Mapping. Grids of 50, 100 and 200 µm (resulting in different signal to noise ratio) were used to calculate maps of the following local metrics: *(i)* average axon diameter within a grid element, *(ii)* number of myelinated axons ranging from 1 to 4 µm in diameter present within a grid element, *(iii)* number of axons ranging from 4 to 8 µm present within a grid element, (*iv*) number of axons ranging from 8 to 12 µm present within a grid element, (*v*) total number of myelinated axons present within a grid element, *(vi)* myelin volume fraction, *(vii)* axon volume fraction, and (*viii*) fiber (= myelin plus axon) volume fraction. Note that we extrapolate the volume of myelin or axons from the area by assuming consistency of these areas along the spinal cord axis. Therefore,

$$Myelin\ Volume\ Fraction(MVF) = N_{myelin}/N_{total}$$

$$Axonal\ Volume\ Fraction\ (AVF) = N_{axon}/N_{total}$$

$$Fiber\ Volume\ Fraction\ (FVF) = (N_{axon} + N_{myelin})/N_{total}$$

with N_j the number of pixels attributed to class j in each grid element (e.g. for a grid of 50 µm and a resolution of 0.13 µm, $N_{total} = (50/0.13)^2 = 150,000\ pixels$).

Atlas registration. In order to identify the different spinal cord pathways, we registered the digital version ($80 \times 80 \times 500\ \mu m^3$) of the Gray's Anatomy (Gray et al., 2005) atlas that is part of the Spinal Cord Toolbox (SCT) (De Leener et al., 2017b; Lévy et al., 2015) using elastic deformation to the 50 µm map. For each sample, the corresponding mid-vertebral level (or slightly shifted when multiples slices were extracted at the same level) of the atlas was extracted, and registered in two steps: an initial affine transformation based on manually selected control points (*cpselect* and *fitgeotrans* functions available in the Matlab image processing toolbox), and a diffeomorphic elastic transformation (SyN) estimated on manually drawn masks of spinal cord with two labels for gray and white matter (command *sct_register_multimodal* from SCT, metric "Mean Squares") (Avants et al., 2011; De Leener et al., 2017b). The elastic transformation (regularized with b-splines, BsplineSyN) was divided into two steps: a first transformation for "smooth" (i.e. global) deformations and a second transformation allowing for more local deformations. Fig. 3 shows an example of the registration framework.

Template creation. Maps of axon morphometry at the downsampled 50, 100, and 200 µm resolutions were registered to the spinal cord PAM50 template (MRI template) (De Leener et al., 2017a). For this transformation (histology to template space), the local deformation step was not included in order to preserve the shape of the inner structures (e.g. gray matter). Missing levels were filled by registration and interpolation of the closest available slices. The nearest superiorly and inferiorly positioned slices were first registered to the missing levels using the white matter masks, then the distance-weighted average was used. Due to the small number of slices at thoracic levels, the template was generated for the full cervical part only.

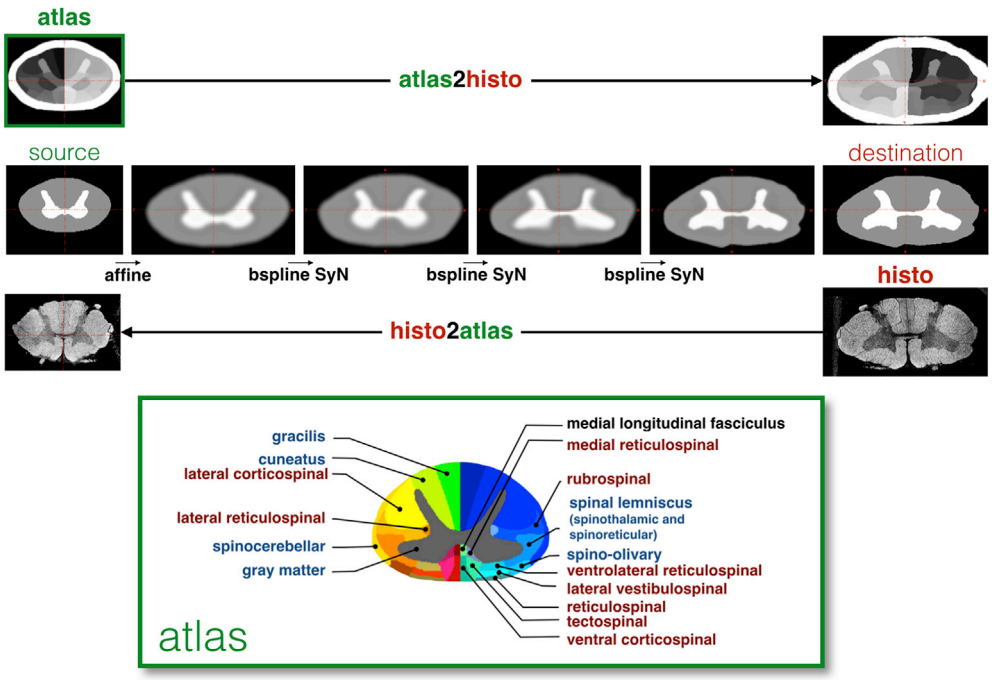

Fig. 3. Registration (top row) of the atlas to histology image ('histo'). Registration was estimated (middle row) based on the masks of white and gray matter of the atlas (source) and histology (destination). Multiple steps were used: affine, and multiple non-linear deformations regularized with bsplines (bspline SyN). The inverse transformation (bottom row) used only smooth deformation in order to keep the shape of internal structures intact.

2.4. Statistics

We used the warped spinal cord atlas in the downsampled histology space to measure the axon morphometry in each tract, and then computed the Pearson correlation coefficient between slices. Maximal laterality difference was assessed using the coefficient of reproducibility (1.96 times the standard deviation of the differences), and statistical significance was computed using a paired *t*-test.

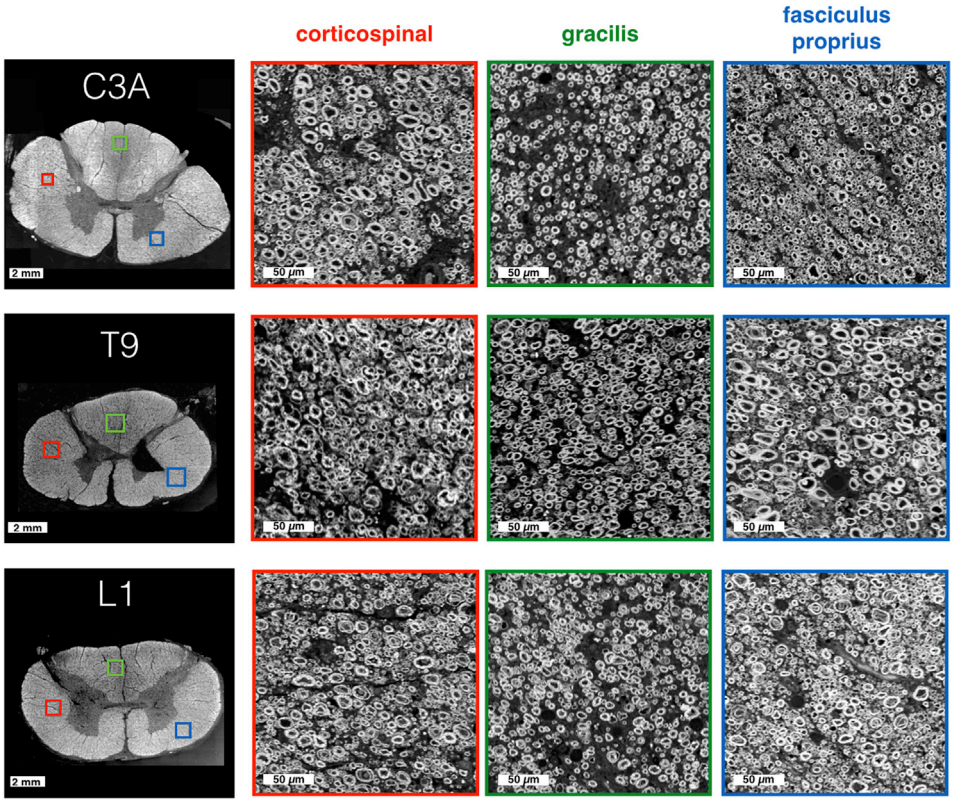

Fig. 4. SEM images of the spinal cord over three pathways (color-coded in red, green and blue), at three spinal levels (C3, T9 and L1). Myelinated axons can easily be distinguished on these raw SEM images.

3. Results

3.1. Whole-slice imaging and overall results

All cervical levels except C8, four thoracic and six lumbar levels were imaged in mosaic, stitched and segmented (see supplementary material 7.3).

A large diversity of microstructure could be observed. For instance, we found a much larger axonal volume fraction in the fasciculus proprius (30% at C3, blue boxes in Fig. 4) than in the gracilis regions (15–20%, green boxes), and the presence of larger axons in the corticospinal tract (median diameter was 3.2 μm, red boxes) than in the gracilis tract (2.5 μm).

3.2. Axon and myelin segmentation

Image and segmentation quality were first qualitatively assessed in several regions. Myelin sheaths were clearly identifiable with relatively sharp borders (Fig. 5b), and the large majority of the axons were detected (Fig. 5c). Using manual segmentation as a ground truth over a small portion of the image ($1 \times 0.5\,mm^2$), the performance of the automatic axon segmentation was evaluated as yielding a sensitivity of 87% and a precision of 78%.

3.3. Microstructural maps

Fig. 6 shows the microstructural maps obtained by processing the segmented histological images on a grid of $100 \times 100\,\mu m^2$ so as to compute measures of fractional volume (axon and myelin volume fraction) as well as to aggregate measures per unit surface (axon diameter, eccentricity, etc.) The resulting maps were consistent across the different slices (see supplementary material 7.4) and were highly symmetrical (see section "Laterality difference").

The axon diameter metric was divided into three density maps (1–4 μm axons, 4–8 μm and 8–12 μm, reported as number of myelinated axons in a $100 \times 100\,\mu m^2$ window). This subdivision clearly reveals the large proprioceptive axons of the cuneatus and spinocerebellar pathways (Niu et al., 2013). Very few axons (less than 5 per $100 \times 100\,\mu m^2$ window) larger than 8 μm were detected, except in the lateral border of the cervical spinal cord (which corresponds approximately to the spinocerebellar pathway).

Axon eccentricity maps represent a combination of two effects: axon compression and not cutting the sample perfectly perpendicular with respect to axons orientation. Maps of axonal eccentricity were highly symmetrical, suggesting that the contrast within the spinal cord is mostly driven by genuine microstructural characteristics (i.e. not compression or cutting artefacts). Some tracts (e.g. dorsal columns) presented axons that were closer to the shape of a circle, indicating that the axons were running straight along the spinal cord. On the contrary, axons in the corticospinal tract were more oblique.

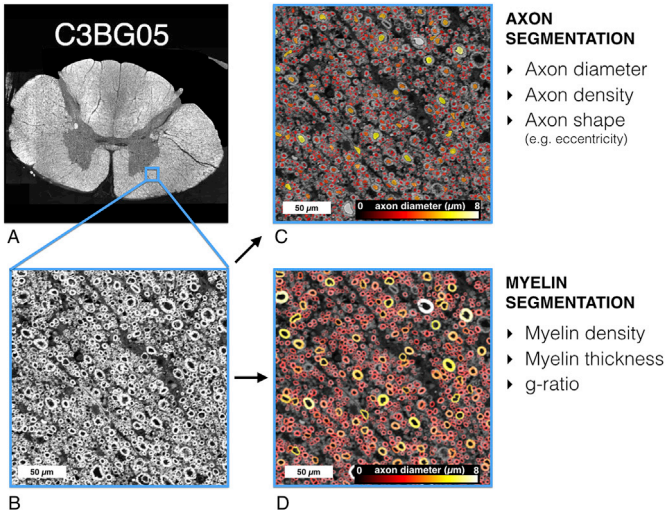

Fig. 5. Extraction of microstructural information. A: Large-scale SEM image after stitching all sub-images of the mosaic together, B: zoomed window of $100 \times 100\,\mu m^2$, C: segmentation of axons and D: segmentation of myelin. The computed morphometric information is listed on the right panel.

The gray matter presented a very different microstructure than the white matter in terms of axonal density and orientation. Because the segmentation software and the correction framework was trained on white matter regions, the accuracy of the measures was compromised. However, a comparison against manual segmentation shows overall satisfactory results over the gray matter as well. See Supplementary material 7.5 for more details.

3.4. Atlas-based analysis

Axon morphometrics were then extracted for each tract using an atlas registration method (Fig. 3). We investigated the variation of axon morphometry with respect to the spinal cord pathway, spinal level and laterality.

3.4.1. Inter-tract variability

In the white matter section of level C5B (Fig. 7), the median axon diameter ranged from 2.3 μm (gray matter) to 3.4 μm (spinocerebellar tract). Median values in other major tracts was: 2.5 (gracilis), 2.6 μm (lateral corticospinal) and 2.9 μm (cuneatus). Axonal volume fraction in C5B white matter varied between 25% in the gracilis tract and 50% in the spino-olivary tract. At C2C level, axon diameter ranged from 2.5 μm (gray matter) to 3 μm (spinocerebellar), and fiber volume fraction ranged from 33% (gracilis) to 50% (lateral vestibulospinal). The distribution of metrics appeared to be relatively broad in a few tracts (e.g. spinocerebellar), which is likely partly due to the presence of spurious outliers caused by partial voluming with the gray matter and/or the background. Despite these artifactual issues, the 95% confidence intervals were overall relatively narrow and revealed significant microstructural differences between tracts.

3.4.2. Effect of spinal level

Slice position was defined in the spinal cord template coordinates (De Leener et al., 2017a). Morphometric properties were averaged in the white matter (all tracts of the registered atlas) and plotted as a function of the slice position (see Fig. 8). Values were consistent across slices and a smoothing spline was plotted to highlight the trends.

The global number of myelinated axons in the whole spinal cord decreased monotonically when going from the brain down the spine (i.e. caudal direction), as illustrated in Fig. 8f. This progressive reduction in axons is due to the ingress (sensory) and egress (motor) branching at successive nerve root levels that continue while descending the spine. This decrease in the number of fibers correlated strongly with the reduction of the spinal cord cross-sectional area (Fig. 8a) ($r = 0.9$, $p = 10^{-7}$) and white matter area (Fig. 8b) ($r = 0.9$, $p = 10^{-8}$), while it correlated moderately with the fiber volume fraction (Fig. 8c) ($r = 0.5$, $p = 10^{-2}$). Note that not all axons originate from the supra-spinal region as some proprioceptive axons only run a few segments and synapse directly within the spinal cord gray matter (Niu et al., 2013).

The myelin volume fraction (Fig. 8e) was relatively constant along the spinal cord, with a difference of only 3% between the lumbar (average of 20%) and cervical levels (23%). Axonal diameter, fiber volume fraction and myelin volume fraction exhibited maximal values between the low cervical levels and the mid-thoracic levels.

3.4.3. Laterality difference

When averaging across all levels, the spinal cord microstructure appeared to be highly symmetrical (see supplementary material 7.6).

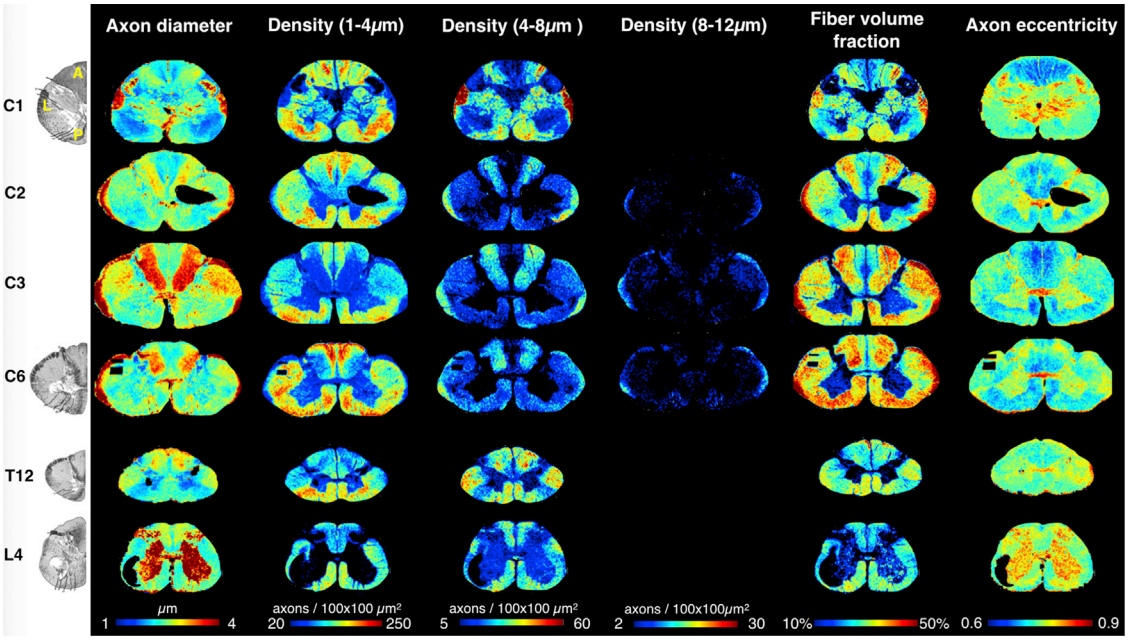

Fig. 6. Maps of axon microstructure. Mean axonal diameter (first column), 1–4 μm density defined as the number of axons having diameters between 1 and 4 μm per $100 \times 100\ \mu m^2$ area unit (second column), 4–8 μm density (third column), 8–12 μm density (fourth column), fiber (axon and myelin) volume fraction (fifth column), and mean axonal eccentricity (sixth column) in grid elements of $100 \times 100\ \mu m^2$ at different spinal levels (rows). These maps can be compared with the manual drawing of cytoarchitecture extracted from (Nieuwenhuys et al., 2007) (left). The spurious black regions visible at C2 and L4 are the result of poor osmium staining (see discussion on "Osmium penetration").

When comparing the left and right tracts on a Bland-Altman plot, we found an average difference between left and right tracts of 0.01 μm for axon diameter, 1% for axon volume fraction and 0.4% for myelin volume fraction. The effect of handedness is further discussed in section 4.1.

3.5. Template

The microstructural maps were registered to the PAM50 spinal cord template developed by De Leener et al. (De Leener et al., 2017a) in order to generate the first MRI-compatible open-access microstructural template of the human cervical spinal cord (see Fig. 9). The combination of regularized SyN transformations and multi-resolution iterative registrations (from 8 to 2 downsampling factors, mesh size of 12) resulted in fairly smooth transitions between adjacent slices. The template covers C1 to C8 spinal levels. A large transition of microstructure and gray matter shape, as well as a lower sampling rate, led to unsatisfying results for levels below C8, hence they were not included in the template.

4. Discussion

In this work we combined high resolution whole-slice histology and automatic axon and myelin segmentation software to produce the first white matter morphometric maps of the entire human spinal cord. While the spinal cord is highly symmetric, different spinal cord pathways exhibit distinct microstructural features.

4.1. Axon morphometry in the spinal cord

As reported in many histological (Nieuwenhuys et al., 2007; Niu et al., 2013) and MRI (Cohen-Adad, 2018; Duval et al., 2017) studies, the human spinal cord presents a large diversity of axon microstructure features (shape, density). For example, axon diameters in the CNS were reported to vary between 0.1 and 10 μm in all species (Perge et al., 2012), with qualitatively larger axons in the spinocerebellar than in the cuneatus, and larger axons in the cuneatus than in the gracilis (Duval et al., 2015; Nieuwenhuys et al., 2007).

In the present study, axon volume fraction at the C3 level was about 30% in the fasciculus proprius vs. 15–20% in the gracilis. Axon diameter values at the C5B level were 2.5 μm (gracilis), 2.9 μm (cuneatus), and 3.4 μm (spinocerebellar) (also see Fig. 7). Aggregate microstructure metrics varied quite substantially along the rostro-caudal axis (see Fig. 8), which can be partly explained by the change in relative cross-sectional area occupied by the different tracts along the cord axis.

To our knowledge, no histological study looked at the right-left difference of microstructure in the spinal cord. Particularly high level of symmetry was reported from microstructural MRI studies of the healthy human spinal cord (Duval et al., 2017, 2015; Lévy et al., 2018, 2015).

In the present study, a high level of symmetry was observed qualitatively (see microstructural maps of Fig. 6), as well as quantitatively (see supplementary material 7.6). We found an average difference between sides (±95% limit of agreement) of 0.01 ± 0.34 μm, $1 \pm 9\%$ and $0.4 \pm 6\%$ for axonal diameter, axon volume fraction and myelin volume fraction respectively. Given that the subject was right-handed, these results suggests that handedness had very little impact on axonal morphometry. This hypothesis needs to be further validated in a larger population, especially by looking at specific levels (as opposed to averaging across all levels as done here). Note that the observed symmetry also supports the idea of a good repeatability and consistency of the entire framework (little bias due to inhomogeneity in staining, polishing or image quality).

The study of axon microstructure in the spinal cord has also been tackled from a neurophysiological angle. Using bioelectrical models and experimental setups, the speed of propagation and the firing rate in myelinated axons were shown to be proportional to the axon diameter (d) (Plonsey and Barr, 2007); while the energy consumption and the fiber volume are proportional to d^2 (Perge et al., 2012). This means that the presence of large axons in the CNS comes at the expense of energy and space efficacy (Perge et al., 2012). The benefits of having large axons are multiple: it provides (i) faster propagation (faster reflexes and better synchronization of the neural impulses) (e.g. squid giant axon), and (ii) higher firing rate (Perge et al., 2012).

The microstructural maps (Fig. 6), and notably the axon diameter maps, reveal a functional organization (Niu et al., 2013). For instance,

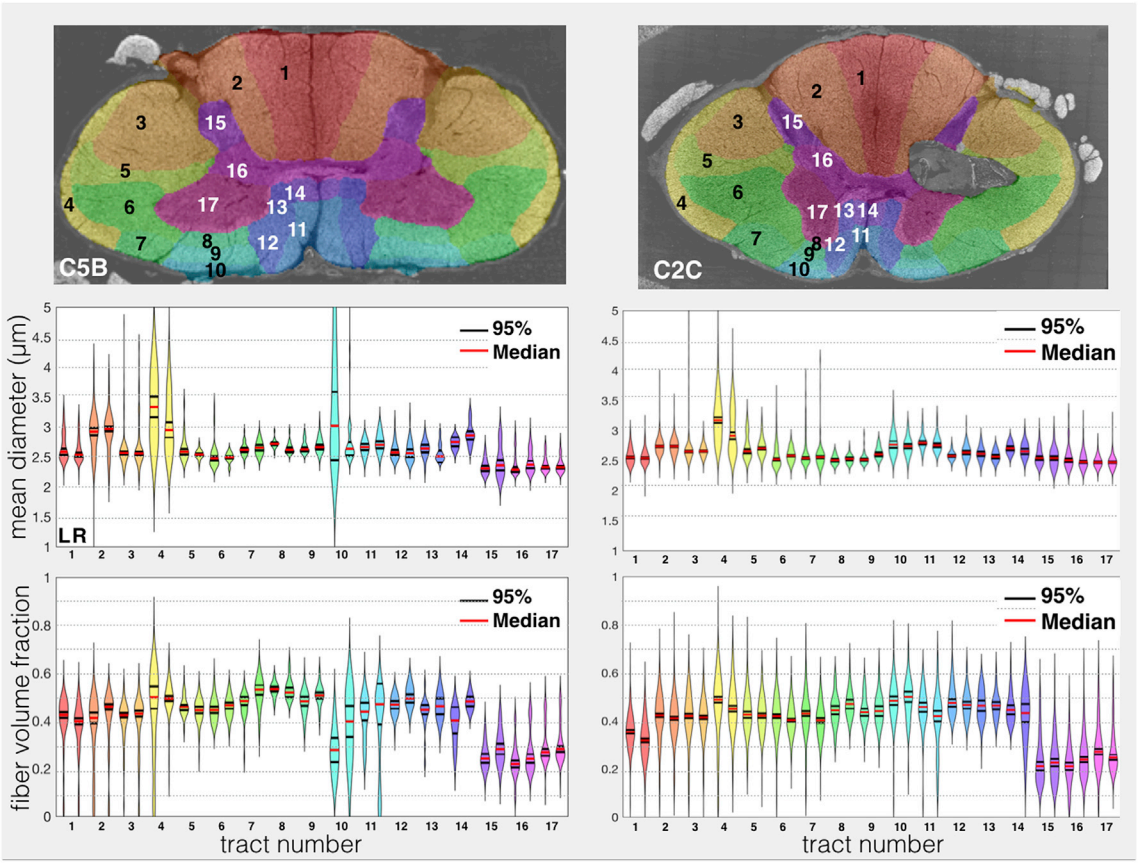

Fig. 7. Atlas-based analysis. The spinal cord white matter atlas (Lévy et al., 2015), built from Gray's Anatomy (Gray et al., 2005), was registered to the histological slices in order to extract axonal morphometry in the following spinal cord pathways (listed in abscissa as "tract number"): 1: gracilis, 2: cuneatus, 3: lateral corticospinal, 4: spinocerebellar, 5: rubrospinal, 6: spinal lemniscus, 7: spino-olivary, 8: ventrolateral reticulospinal, 9: lateral vestibulospinal, 10: ventral reticulospinal, 11: ventral corticospinal, 12: tectospinal, 13: medial reticulospinal, 14: medial longitudinal fasciculus, 15: Gray Matter dorsal horn, 16: Gray matter intermediate zone, 17: Gray matter ventral horn. For each pathway, the distribution of the pixel-averaged (mean) axonal diameter (middle row) and fiber volume fraction (bottom row) in the left (L) and right (R) hemicord are presented. The median (red lines) and 95% confidence interval (black lines) show that each tract presents very specific microstructures. Most tracts exhibit a fairly homogeneous microstructure as shown by the narrow distributions.

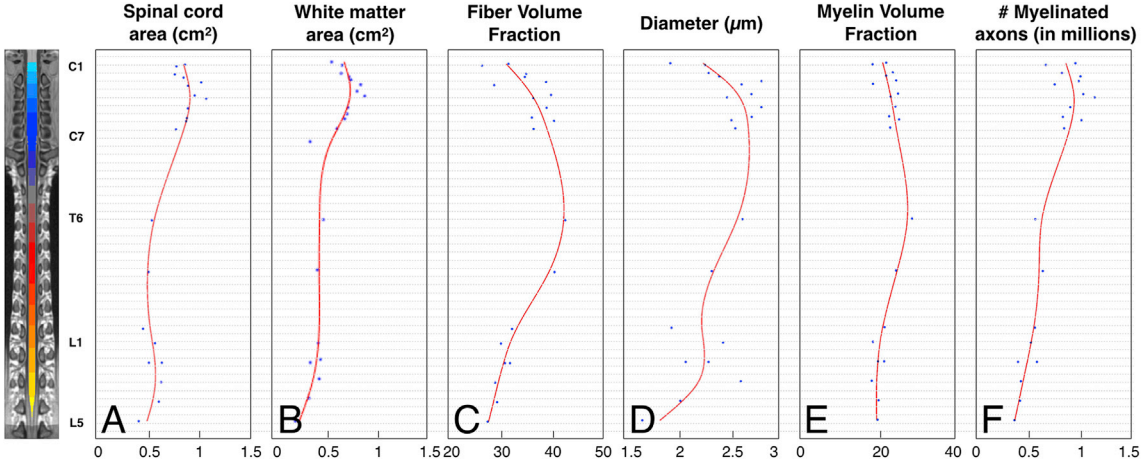

Fig. 8. Evolution of the axonal morphometry along the spinal cord. Morphometric properties were averaged in the white matter for each sample (blue dots), and a smoothing spline (red line) was fitted for visualization.

the contrast between the gracilis and the cuneatus in the dorsal column is the result of the presence of two types of afferent sensory axons with different caliber: the large proprioceptive (>4 μm) and smaller mechanoreceptive axons (Niu et al., 2013) (formerly interpreted as a "somatotopic organization" of the dorsal column). Similarly, the relatively higher number of large axons (4–8 μm) at L4 and T12 compared to the cervical levels (Fig. 6, column 3), is likely caused by the relative increase in the number of small axons as we go caudally along the spine. Indeed, large proprioceptive fibers enter as low as the sacral segments but generally synapse with the gray matter about five segments upward,

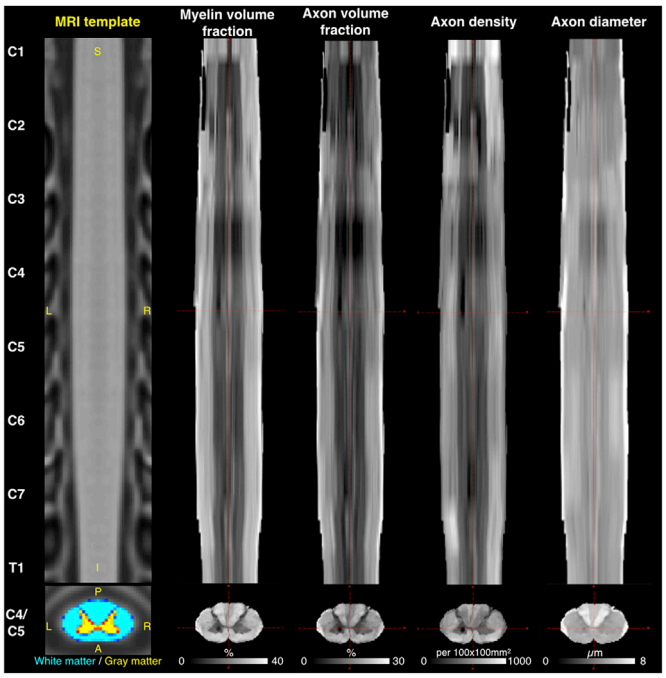

Fig. 9. Microstructural template of the spinal cord. Coronal (top) and axial (bottom) view of the generated template. Histological slices were registered at the corresponding vertebral levels of the PAM50 MRI template (left), and then interpolated between slices using non-linear deformations. The resulting template shows fairly smooth transitions between slices. Note that "axon number" refers to myelinated axons only. The white/gray matter overlaid on the axial view of the MRI template is a probabilistic representation of the spinal cord internal structure (Lévy et al., 2015) and shows similar morphometry when compared to the histology-based atlases.

whereas smaller mechanoreceptive axons enter the dorsal column at higher levels and terminate up to the medulla oblongata (Niu et al., 2013).

4.2. Challenges of tissue preparation

4.2.1. Fixation procedure

The first challenge in all histological studies on post-mortem tissue is the preservation of the tissue and, in particular, the integrity of the myelin. Based on what is typically used in literature (Saliani et al., 2017), here we used a mixture of glutaraldehyde and paraformaldehyde (PFA). Paraformaldehyde is used for its fast chemical reactiveness and deep tissue penetration, and glutaraldehyde for its strong cross-linking. Various concentrations of glutaraldehyde (0.5–4%) can be found in the literature (Biedenbach et al., 1986; Firmin et al., 2014; Ralston et al., 1987), and a compromise is required between tissue shrinkage and microstructure preservation.

Although PFA leads to tissue shrinkage, the effect is more dramatic with higher glutaraldehyde concentration (Hayat, 2000). Due to the uncertainty on the impact of this concentration on axonal morphometry, we decided to use three concentrations (0, 0.5 and 2%). No particular differences were found between the three fixatives mixtures on the metrics reported, as seen in supplementary material 7.4, suggesting that the effect of shrinkage is negligible compared to the variation of microstructure between regions (slices and tracts). Although different fixatives were used, trends were clearly observed when looking at the effect of spinal level (Fig. 8).

4.2.2. Myelin integrity

Myelin integrity was not perfectly preserved, as shown by the abnormally low g-ratio observed (see supplementary material 7.7). This is unfortunately difficult to avoid when perfusion fixation cannot be performed. This observation motivated the report of metrics that are not impacted much by this issue (see discussion about accuracy).

4.2.3. Osmium tetroxide penetration

At the end of the staining procedure, some slices presented regions of incomplete osmium staining and/or small cracks on the surface (see figure S3, white arrows). In some cases these issues were caused by excessively deep cutting or by the presence of air bubbles which prevented good penetration of the epoxy resin. Osmium tetroxide only penetrates a few hundred microns within the tissue (Hua et al., 2015), making it difficult to ensure a good uniform staining across such large samples. In order to prevent the surface to be polished being located deeper than the osmium penetration (roughly 200 µm), the surface was exposed by cutting it at various angles. Another strategy would be to improve the osmium penetration by using recently published protocols (Hua et al., 2015; Mikula and Denk, 2015).

4.2.4. Cutting

Because the samples were embedded in hard epoxy, a particularly hard Carbide-Tungsten blade was used. The thickness of the cutting was limited to 20 µm and the speed of cutting was limited to reduce the forces on the blade. The hard epoxy protected the tissue and its microstructure correctly, and no cutting artefact (e.g. compression) was observed. After cutting, however, the surface was not sufficiently well polished, leading to strong artefacts during the imaging. Additional polishing procedure was thus necessary.

4.3. Challenges of image acquisition

4.3.1. Timing

Using the present method, at a resolution of 130 nm, it took about 8 h to image each slice. Multi-beam solutions (Dellemann et al., 2015) are encouraging strategies for reducing scanning time without compromising image resolution, should larger scale studies be undertaken.

4.3.2. Focus

The images were obtained in low magnification mode. This choice was motivated by the large field of view and the large depth of field of this mode. Still, one slice (T4 in supplementary material 7.3) suffered from poor focus and hence needed to be discarded from the analysis. We experienced a loss of focus when the SEM vacuum level was slightly altered. We therefore used liquid nitrogen and had to refill the nitrogen during the scan in order to maintain the stability of the vacuum.

4.3.3. Resolution limit

In this study, in order to increase the backscattered signal of the electrons as well as to increase the speed of acquisition, we used a relatively high voltage (i.e. 15 keV). This choice resulted in a reduction of the structural details (due to higher penetration, and thus larger electron interaction volume). We estimated the effective spatial resolution by computing the intensity profile of a few large axons using ImageJ. Using the Rayleigh criterion, axons smaller than 1 µm internal diameter (i.e. about 8 pixels at 129 nm pixel size) appear as solid dots instead of open circles and thus could not reliably be labeled as "axon" by AxonSeg. In order to prevent strong biases in our results, we decided to discard axons smaller than 1 µm from the results. Because it is still unclear from the literature what is the proportion of myelinated axons that are smaller than 1 µm in diameter (Saliani et al., 2017), subsequent studies involving transmission electron microscopy should be performed in human samples. Alternatively, better resolution could be achieved with scanning electron microscopy by reducing the voltage and by using the high magnification mode, but that would be at the expense of scanning time, contrast to noise ratio, and/or shorter depth of field. We note however, that AxonSeg also failed to detect some axons in the 2–3 µm range (see figure S7). To compensate for these "apparent" false negatives (2–3 µm), quantitative

maps were calibrated using manual segmentation (see figure S2).

4.3.4. 2D imaging

In this work, 2D images of the spinal cord were obtained, based on the assumption of relatively straight axons running along the spinal cord (axons orientation is dispersed up to 28° in the spinal cord) (Grussu et al., 2016). This assumption, however, would not hold in brain regions with a large orientation dispersion; rather 3D scanning electron microscopy (Abdollahzadeh et al., 2017; Knott et al., 2008) or 3D optical imaging (Bégin et al., 2014; Susaki and Ueda, 2016) could be considered in these cases. Note that 3D imaging will also make the dataset a hundredfold larger, thereby rendering acquisition and processing time extremely lengthy.

The effect of axon orientation on our measurements is reported in supplementary material 7.8. Axon diameter is overestimated by less than 10% for axons running with an angle of 35° with respect to the spinal cord main axis. Fiber volume fraction and myelin volume fraction should not be impacted.

Interestingly, the shape of the axons (i.e. elliptical shapes) provides some information about the third dimension (direction of the fibers). This interpretation could be questioned because axonal compression is a confounding factor that cannot be separated easily. However, maps of axonal eccentricity were highly symmetrical, suggesting that the contrast within the spinal cord reveals microstructural information (as opposed to compression, shearing or cutting artefacts that would result in local or asymmetric contrasts). Note that the average axon eccentricity measured in some regions (up to 0.7) corresponds to angles up to 45°. Future investigations (e.g. with sagittal cutting of the spinal cord, or 3D electron microscopy) are necessary to elucidate the contribution of non-oblique tracts vs. non cylindrical axons to the observed high eccentricity.

Note that the axon eccentricity measured in some regions (up to 0.7) correspond to excessively high angles (45°), which shows that axons are not perfectly cylindrical.

4.4. Other challenges

4.4.1. Staining

Finally, it should be mentioned that the current protocol is blind to unmyelinated axons and glial cells due to the use of osmium, which only stains for myelin. These structures can be seen at a lower voltage and following an advanced osmium staining method (Hua et al., 2015), but would result in a lower signal to noise ratio and more complex images, thereby requiring the development of more advanced segmentation software. However, the proportion of unmyelinated axons in the spinal cord white matter is less than 1% (at least in the corticospinal tract) according to both Firmin et al. (2014) and Wada et al. (2001) (in the macaque and human respectively).

4.4.2. Inter-subject variability

This study is based on a single spinal cord extracted from a 71 year old woman. The microstructure is known to change as a function of age (Branzoli et al., 2016; Watson et al., 2009, p. 39) and sex (Cerghet et al., 2006): for instance, lower axonal density has been reported in elderly people (Watson et al., 2009, p. 39), and conduction time and amplitude are reduced (Esposito et al., 1996). However, these finding were based on indirect measures of the microstructure (MRI or electromyography), or were assessed in the small animals. In order to quantitatively assess the effect of age in the microstructure metrics, we recommend using direct measures as done here. This could be the subject of future investigations.

4.5. Accuracy of the measurement

As summarized in (Saliani et al., 2017), axon morphometry measured with histology varies greatly between studies. For instance, the axonal count may vary between 8000 and 100,000 axons/mm^2 in the pyramidal tract, or the proportion of axons smaller than 1 μm may vary between 30% and 90%. These strong variations result from (i) staining issues, that can cause confounds (e.g. between axons and glial cells) (Wada et al., 2001) or render poorly stained axons hardly visible (Hua et al., 2015), (ii) the resolution limit of the imaging system that make the detection of the smallest axons impossible (Firmin et al., 2014) and introduce a constant bias due to the point spread function, and (iii) tissue degradation (e.g. unwrapped myelin). Additionally, segmentation performance (sensitivity, specificity, accuracy) and ambiguities in the methods (myelinated-only or all fibers?) make the comparison with other studies difficult.

Values reported in this study concern only myelinated axons that are larger than 1 μm (see resolution limit). Segmentation bias was limited by using an automatic segmentation method combined with a correction framework detailed in supplementary material 7.2.

4.5.1. Axonal density

We found between 10,000 and 20,000 axons/mm^2 in the corticospinal tract (i.e. pyramidal tract), depending on the vertebral level. We thus confirm the observation of (Wada et al., 2001): pioneer studies such as (Lassek and Rasmussen, 1940) overestimated by five to ten-fold (100,000 axons/mm^2 was reported) the number of axons due to staining issues. Note that Wada et al. (2001) reported a value relatively close to our results: about 9000 axons/mm^2.

4.5.2. Axon diameter

Axon diameter accuracy can be impacted by the over-segmentation of the myelin, axonal compression, and the orientation of the axons.

The over-segmentation of the myelin resulted in a constant underestimation of the axonal diameter by a fraction of a micron (see discussion about “resolution limit”).

The axon diameter overestimation for oblique axons was formulated in supplementary material 7.8. For the majority of the axons (angle $<40°$), the overestimation was limited to about 10%. Also, AxonSeg filters highly oblique axons (limiting obliquity to at most 70°) based on their minor to major axis ratio.

4.5.3. Myelin volume fraction and fiber volume fraction

The myelin volume fraction in the white matter (20–30%, see template) was close to what has been measured by other groups using transmission electron microscopy in the brain (25–30%) (Mottershead et al., 2003; Ong and Wehrli, 2011; Perge et al., 2009). Note that, contrary to transmission electron microscopy studies, we segment the entire spinal cord and not only small white matter regions, and our reported MVF values can be lower because we take into account the presence of veins and fissures.

As discussed earlier (section “Tissue preparation”), the myelin is not perfectly dense (i.e. with no space between layers of the myelin sheath), especially for large axons. Fiber and myelin volume fraction were the most impacted metrics by this limitation. In order to estimate the overestimation of myelin volume fraction, we computed the myelin volume fraction assuming a constant g-ratio of 0.7 for all axons. With this assumption, the myelin volume fraction (MVF) can be related to the axon volume fraction (AVF) as follow: $MVF = (1/g^2 - 1) \times AVF = 1.04 \times AVF$. With this approach, we found a linear relationship (data not shown) between our reported MVF value and MVF values obtained assuming a g-ratio of 0.7: $MVF_{reported} = 0.68 \times MVF_{g=0.7}$. Likewise, the fiber volume fraction (FVF = AVF + MVF) can be computed directly from AVF: $FVF_{reported} = 0.76 \times FVF_{g=0.7}$. As a result, although the reported values for myelin volume fraction and fiber volume fraction are meaningful for inter-tract and inter-slice study, readers must be aware of this upward bias. Further work will need to improve myelin integrity or use TEM studies on well preserved axons (with compact myelin) to refine this calibration.

5. Conclusion

We present the first microstructural template of the human spinal cord based on histology, registered on the spinal cord MRI template

PAM50. To generate this template, we developed a framework that includes whole slice electron microscopy, automatic axon segmentation and coregistration of the slices. The template can be used to revise biophysical models and spinal cord atlases, and validate non-invasive techniques that measure spinal cord microstructure.

Acknowledgements

We would like to thank Micheline Fortin and the other employees of the histology department of the Institute for Research in Immunology and Cancer (University of Montreal, QC, Canada), Diane Gingras from the electron microscopy department of the University of Montreal, as well as Irène Londono, Monica Nelea and Anik Chevrier. Their help and advice for the preparation of the samples greatly contributed to the success of this work. We would also like to thank the members of the Center for Characterization and Microscopy of Materials $(CM)^2$, notably Nicole MacDonald, Philippe Plamondon, Jean-Philippe Masse and Gilles L'Espérance, for their support on the polishing and scanning of the spinal cord samples. Finally, we would like to thank the reviewers for their thorough proofreading and feedback. Their comments greatly improved the quality of the manuscript.

Funded by the MS Society of Canada [EGID 2370], the Canada Research Chair in Quantitative Magnetic Resonance Imaging (JCA), the Canadian Institutes of Health Research [CIHR FDN-143263], the Canada Foundation for Innovation [32454, 34824], the Fonds de Recherche du Québec - Santé [28826], the Fonds de Recherche du Québec - Nature et Technologies [2015-PR-182754], the Natural Sciences and Engineering Research Council of Canada [435897-2013], IVADO, TransMedTech and the Quebec BioImaging Network.

Appendix A. Supplementary data

Supplementary data to this article can be found online at https://doi.org/10.1016/j.neuroimage.2018.10.033.

References

Abdollahzadeh, A., Belevich, I., Jokitalo, E., Tohka, J., Sierra, A., 2017. 3D Axonal Morphometry of White Matter. BioRxiv. https://doi.org/10.1101/239228.

Avants, B.B., Tustison, N.J., Song, G., Cook, P.A., Klein, A., Gee, J.C., 2011. A reproducible evaluation of ANTs similarity metric performance in brain image registration. Neuroimage 54, 2033–2044.

Begin, S., Dupont-Therrien, O., Bélanger, E., Daradich, A., Laffray, S., De Koninck, Y., Côté, D.C., 2014. Automated method for the segmentation and morphometry of nerve fibers in large-scale CARS images of spinal cord tissue. Biomed. Opt. Express, BOE 5, 4145–4161.

Biedenbach, M.A., De Vito, J.L., Brown, A.C., 1986. Pyramidal tract of the cat: axon size and morphology. Exp. Brain Res. 61, 303–310.

Cohen-Adad, J., 2018. Microstructural imaging in the spinal cord and validation strategies. Neuroimage. https://doi.org/10.1016/j.neuroimage.2018.04.009.

Cohen Adad, J., Wheeler Kingshott, C., 2014. Quantitative MRI of the Spinal Cord. Elsevier Science.

De Leener, B., Fonov, V.S., Collins, D.L., Callot, V., Stikov, N., Cohen-Adad, J., 2017a. PAM50: unbiased multimodal template of the brainstem and spinal cord aligned with the ICBM152 space. Neuroimage 165, 170–179.

De Leener, B., Lévy, S., Dupont, S.M., Fonov, V.S., Stikov, N., Louis Collins, D., Callot, V., Cohen-Adad, J., 2017b. SCT: spinal Cord Toolbox, an open-source software for processing spinal cord MRI data. Neuroimage 145, 24–43.

Dellemann, G., Kemen, T., Eberle, A., Garbowski, T., Malloy, M., Bunday, B., Thiel, B., Zeidler, D., 2015. Advances in multi-beam SEM technology for high-throughput defect inspection. In: Carl Zeiss Microscopy GmbH and SEMATECH.

Demyer, W., 1959. Number of axons and myelin sheaths in adult human medullary pyramids; study with silver impregnation and iron hematoxylin staining methods. Neurology 9, 42–47.

Dula, A.N., Gochberg, D.F., Valentine, H.L., Valentine, W.M., Does, M.D., 2010. Multiexponential T2, magnetization transfer, and quantitative histology in white matter tracts of rat spinal cord. Magn. Reson. Med. 63, 902–909.

Duval, T., Lévy, S., Stikov, N., Campbell, J., Mezer, A., Witzel, T., Keil, B., Smith, V., Wald, L.L., Klawiter, E., Cohen-Adad, J., 2017. g-Ratio weighted imaging of the human spinal cord in vivo. Neuroimage 145, 11–23.

Duval, T., McNab, J.A., Setsompop, K., Witzel, T., Schneider, T., Huang, S.Y., Keil, B., Klawiter, E.C., Wald, L.L., Cohen-Adad, J., 2015. In vivo mapping of human spinal cord microstructure at 300mT/m. Neuroimage 118, 494–507.

Esposito, F., Malgrati, D., Veicsteinas, A., Orizio, C., 1996. Time and frequency domain analysis of electromyogram and sound myogram in the elderly. Eur. J. Appl. Physiol. Occup. Physiol. 73, 503–510.

Firmin, L., Field, P., Maier, M.A., Kraskov, A., Kirkwood, P.A., Nakajima, K., Lemon, R.N., Glickstein, M., 2014. Axon diameters and conduction velocities in the macaque pyramidal tract. J. Neurophysiol. 112, 1229–1240.

Gray, H., 1867. Anatomy, Descriptive and Surgical. Henry C. Lea.

Gray, H., Standring, S., Ellis, H., Berkovitz, B.K.B., 2005. Gray's Anatomy: the Anatomical Basis of Clinical Practice, Gray's Anatomy. Elsevier Churchill Livingstone.

Grussu, F., Schneider, T., Yates, R.L., Zhang, H., Wheeler-Kingshott, C.A.M.G., DeLuca, G.C., Alexander, D.C., 2016. A framework for optimal whole-sample histological quantification of neurite orientation dispersion in the human spinal cord. J. Neurosci. Methods 273, 20–32.

Haralick, R.M., Shapiro, L.G., 1992. Computer and Robot Vision, first ed. Addison-Wesley Longman Publishing Co., Inc., Boston, MA, USA.

Hayat, M.A., 2000. Principles and Techniques Electron Microscopy Biological Applications | Biological Imaging, fourth ed. Cambridge University Press.

Hua, Y., Laserstein, P., Helmstaedter, M., 2015. Large-volume en-bloc staining for electron microscopy-based connectomics. Nat. Commun. 6, 7923.

Knott, G., Marchman, H., Wall, D., Lich, B., 2008. Serial section scanning electron microscopy of adult brain tissue using focused ion beam milling. J. Neurosci. 28, 2959–2964.

Lassek, A.M., 1945. The human pyramidal tract: XI. Correlation of the babinski sign and the pyramidal syndrome. Arch NeurPsych 53, 375–377.

Lassek, A.M., Rasmussen, G.L., 1940. A comparative fiber and numerical analysis of the pyramidal tract. J. Comp. Neurol. 72, 417–428.

Lévy, S., Benhamou, M., Naaman, C., Rainville, P., Callot, V., Cohen-Adad, J., 2015. White matter atlas of the human spinal cord with estimation of partial volume effect. Neuroimage 119, 262–271.

Lévy, S., Guertin, M.-C., Khatibi, A., Mezer, A., Martinu, K., Chen, J.-I., Stikov, N., Rainville, P., Cohen-Adad, J., 2018. Test-retest reliability of myelin imaging in the human spinal cord: measurement errors versus region- and aging-induced variations. PloS One 13, e0189944.

Mikula, S., Binding, J., Denk, W., 2012. Staining and embedding the whole mouse brain for electron microscopy. Nat. Methods 9, 1198–1201.

Mikula, S., Denk, W., 2015. High-resolution whole-brain staining for electron microscopic circuit reconstruction. Nat. Methods 12, 541–546.

Mottershead, J.P., Schmierer, K., Clemence, M., Thornton, J.S., Scaravilli, F., Barker, G.J., Tofts, P.S., Newcombe, J., Cuzner, M.L., Ordidge, R.J., McDonald, W.I., Miller, D.H., 2003. High field MRI correlates of myelin content and axonal density in multiple sclerosis–a post-mortem study of the spinal cord. J. Neurol. 250, 1293–1301.

Nieuwenhuys, R., Voogd, J., van Huijzen, C., 2007. The Human Central Nervous System: a Synopsis and Atlas. Springer.

Niu, J., Ding, L., Li, J.J., Kim, H., Liu, J., Li, H., Moberly, A., Badea, T.C., Duncan, I.D., Son, Y.-J., Scherer, S.S., Luo, W., 2013. Modality-based organization of ascending somatosensory axons in the direct dorsal column pathway. J. Neurosci. 33, 17691–17709.

Ong, H.H., Wehrli, F.W., 2011. Assessment of axon diameter distribution in mouse spinal cord with q-space imaging. In: Proceedings of the 20th Annual Meeting of ISMRM, Montréal.

Perge, J.A., Koch, K., Miller, R., Sterling, P., Balasubramanian, V., 2009. How the optic nerve allocates space, energy capacity, and information. J. Neurosci. 29, 7917–7928.

Perge, J.A., Niven, J.E., Mugnaini, E., Balasubramanian, V., Sterling, P., 2012. Why do axons differ in caliber? J. Neurosci. 32, 626–638.

Plonsey, R., Barr, R.C., 2007. Bioelectricity: a Quantitative Approach. Springer Science & Business Media.

Preibisch, S., Saalfeld, S., Tomancak, P., 2009. Globally optimal stitching of tiled 3D microscopic image acquisitions. Bioinformatics 25, 1463–1465.

Ralston, D.D., Milroy, A.M., Ralston 3rd, H.J., 1987. Non-myelinated axons are rare in the medullary pyramids of the macaque monkey. Neurosci. Lett. 73, 215–219.

Saliani, A., Perraud, B., Duval, T., Stikov, N., Rossignol, S., Cohen-Adad, J., 2017. Axon and myelin morphology in animal and human spinal cord. Front. Neuroanat. 11, 129.

Schindelin, J., Arganda-Carreras, I., Frise, E., Kaynig, V., Longair, M., Pietzsch, T., Preibisch, S., Rueden, C., Saalfeld, S., Schmid, B., Tinevez, J.-Y., White, D.J., Hartenstein, V., Eliceiri, K., Tomancak, P., Cardona, A., 2012. Fiji: an open-source platform for biological-image analysis. Nat. Methods 9, 676–682.

Sommer, C., Straehle, C., Köthe, U., Hamprecht, F.A., 2011. Ilastik: interactive learning and segmentation toolkit. In: 2011 IEEE International Symposium on Biomedical Imaging: from Nano to Macro, pp. 230–233.

Susaki, E.A., Ueda, H.R., 2016. Whole-body and whole-organ clearing and imaging techniques with single-cell resolution: toward organism-level systems biology in mammals. Cell Chem Biol 23, 137–157.

Verhaart, W.J., 1962. The pyramidal tract. Its structure and functions in man and animals. World Neurol. 3, 43–53.

Wada, A., Goto, J., Goto, N., Kawamura, N., Matsumoto, K., 2001. Are there one million nerve fibres in the human medullary pyramid? Okajimas Folia Anat. Jpn. 77, 221–224.

Walhovd, K.B., Johansen-Berg, H., Káradóttir, R.T., 2014. Unraveling the secrets of white matter–bridging the gap between cellular, animal and human imaging studies. Neuroscience 276, 2–13.

Watson, C., Paxinos, G., Kayalioglu, G., 2009. The Spinal Cord: a Christopher and Dana Reeve Foundation Text and Atlas. Academic Press, Cambridge.

Zaimi, A., Duval, T., Gasecka, A., Côté, D., Stikov, N., Cohen-Adad, J., 2016. AxonSeg: open source software for axon and myelin segmentation and morphometric analysis. Front. Neuroinf. 10, 37.

Zaimi, A., Wabartha, M., Herman, V., Antonsanti, P.-L., Perone, C.S., Cohen-Adad, J., 2018. AxonDeepSeg: automatic axon and myelin segmentation from microscopy data using convolutional neural networks. Sci. Rep. 8, 3816.